The Effect of Atmospheric Stability on Microwave Excess Emissivity Due to Wind

Jude C. Giampaolo and Christopher S. Ruf, *Fellow, IEEE*

***Abstract*—The excess microwave emissivity of the ocean surface due to winds at nadir incidence is derived from the TOPEX microwave radiometer and altimeter together with ocean surface data. The sensitivity of emissivity to wind speed is found to depend strongly on the air–sea temperature difference.**

***Index Terms*—Emission, microwave radiometry, sea.**

I. Introduction

One empirical model relating ocean emissivity to surface wind speed is Wilheit [8]

$$\begin{aligned}\varepsilon_{tot} &= \varepsilon_{spec} + 0.0005 \times W \ @ \ W \leq 7 \ \frac{\text{m}}{\text{s}} \\ &= (\varepsilon_{spec} + 0.0035)(1 - f_s) + f_s \ @ \ W > 7 \ \frac{\text{m}}{\text{s}} \end{aligned} \quad (1)$$

where

ε_{tot} total emissivity;
ε_{spec} specular emissivity;
W wind speed in m/s.

and f_s, the effective fractional foam coverage, is given by

$$\begin{aligned} f_s &= a\left(1 - e^{-f/f_0}\right)(W - 7) \ @ \ W \geq 7 \ \frac{\text{m}}{\text{s}} \\ f_s &= 0 \ @ \ W < 7 \ \frac{\text{m}}{\text{s}} \end{aligned} \quad (2)$$

where $a = 0.006$ s/m, f is the frequency in GHz, $f_0 = 7.5$ GHz, and W is the wind speed in m/s. From (1) and (2), it can be seen that emissivity increases linearly with wind at a lower rate below 7 m/s when foam is not present and at a higher rate above 7 m/s when it is. The rate of increase in emissivity with wind will be referred to as the *wind slope*. Our intent in this work is to independently evaluate the magnitude and behavior of the wind slope by assembling coincident estimates of emissivity from a radiometer and of wind speed from a co-located altimeter. In particular, we examine the dependence of the wind slope on the stability condition at the ocean surface via the air–sea temperature difference.

II. Forward Model and Estimation of Emissivity

A useful form of the radiative transfer equation for our purposes is given by

$$T_b = T_u + T_e e^{-\tau} + T_r e^{-\tau} \quad (3)$$

where

T_b brightness temperature measured from orbit looking down at the Earth's surface;
T_u upwelling brightness from the atmosphere;
T_e surface flux;
T_r reflected brightness by the surface from the atmosphere;
τ opacity of the atmosphere.

The surface flux is the product of the surface temperature and surface emissivity or

$$T_e = \varepsilon T_s \quad (4)$$

where ε is surface emissivity, and T_s is sea surface temperature. The reflected brightness is the fraction of the downwelling brightness that is reflected by the Earth's surface, or

$$T_r = (1 - \varepsilon) T_d \quad (5)$$

where T_d is the downwelling brightness from the atmosphere and cold space. Using (4) and (5) to solve for ε in (3) gives

$$\varepsilon = \frac{T_b - T_u - T_d e^{-\tau}}{(T_s - T_d) e^{-\tau}}. \quad (6)$$

It is possible to estimate the sea surface emissivity with (6) using quantities that can either be obtained directly from satellite measurements or approximated with satisfactory accuracy.

TABLE I
Coefficients for Opacity Estimated From Path Delay. Resulting Opacity in Units of Np Given Path Delay in Units of Centimeters. See (9)

Frequency (GHz)	a_0	a_1	a_2
18	1.4201E-02	1.9601E-03	-3.1761E-06
21	1.6383E-02	7.0913E-03	3.0645E-05
37	5.0703E-02	2.1196E-03	2.5978E-05

III. Data From the TOPEX Mission

Data for use in estimating the sea surface emissivity were obtained from the TOPEX satellite. Brightness temperatures at the three frequencies 18, 21, and 37 GHz at a nadir incidence angle are measured by the onboard TOPEX Microwave Radiometer (TMR) [5] and wind speed is estimated using cross-section data from the radar altimeter [7].

The data used cover a period from January 1, 1997 to December 31, 1997. Data were filtered to remove conditions that impede the retrieval of an accurate estimate of sea surface emissivity. Data with bad quality flags were discarded. The flags catch blatant processing problems. Additionally, sea surface temperature, T_s, was restricted to be greater than 275 K. T_s was estimated from monthly mean ocean temperature data generated from several Advanced Very High Resolution Radiometer (AVHRR) instruments. The reported wet path delay was chosen to be 8 cm or less. Higher path delays lead to greater errors in both the estimation of opacity and the correction of estimated emissivity for atmospheric conditions. The radar derived wind speed must be less than 30 m/s and the amount of liquid water, as calculated by the TMR, must be zero. In addition, no two consecutive otherwise valid points were allowed to be closer than 400 km along the ground track. This was done to increase the independence of samples. After all filtering, approximately 50 000 measurements remain.

Using (6), it is possible to estimate emissivity provided the following values are known: T_b, T_u, T_d, T_s, and τ. T_b is measured directly by the TMR. These brightness temperatures were extracted from the TOPEX archives except for the 18 GHz channel. Due to a known calibration error in the 18 GHz TMR channel, the brightness at 18 GHz in 1997 is a constant 1.1 K too high [2]. This offset also alters the retrieved path delay value. The TOPEX value is approximately 5.2 mm too small and must also be corrected [4].

Manuscript received August 29, 2000; revised July 6, 2001.

J. C. Giampaolo is with the Department of Electrical Engineering, Pennsylvania State University, University Park, PA 16802 USA.

C. S. Ruf is with the Department of Atmospheric, Oceanic and Space Sciences, University of Michigan, Ann Arbor, MI 48109 USA (e-mail: cruf@umich.edu).

Publisher Item Identifier S 0196-2892(01)08842-8.

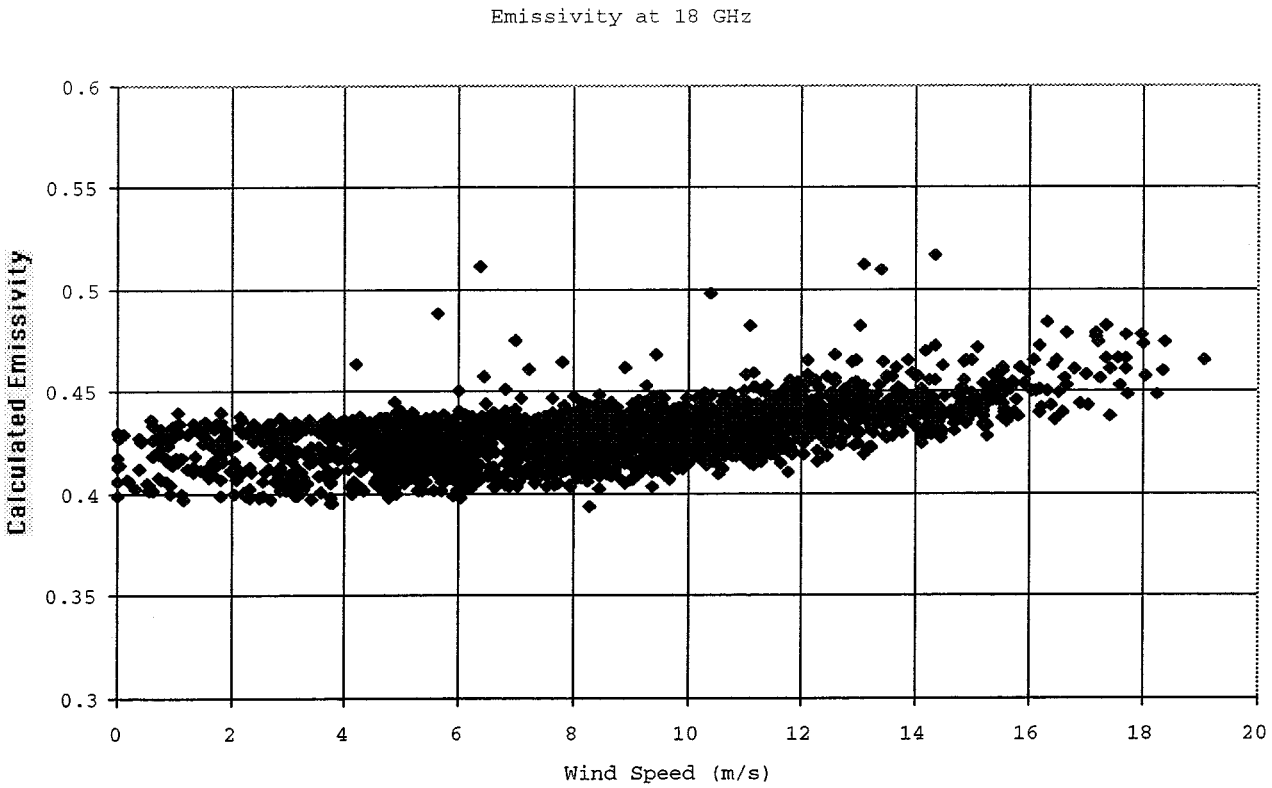

Fig. 1. Ocean surface emissivity at 18 GHz as a function of wind speed. Shown are 2500 representative samples from the one-year data base of $\sim$ 50 000 measurements. Note the increase in sensitivity to wind near 7 m/s with the onset of foaming.

T_u and T_d are estimated from the surface temperature. [6] found that the effective radiating temperature of the atmosphere under normal conditions could be well approximated by

$$T_u \approx (1 - e^{-\tau})(T_s - 14.6) \tag{7}$$

$$T_d \approx (1 - e^{-\tau})(T_s - 13.0). \tag{8}$$

Opacity was estimated from the TOPEX retrieved path delay. For atmospheric conditions that do not have liquid water and have low water vapor content it is possible to estimate the atmospheric opacity accurately with a simple quadratic series

$$\tau = \sum_{i=0}^{2} a_i \, (pd)^i \, . \tag{9}$$

The coefficients in the series are frequency dependent and are given in Table I. These coefficients were generated using a training set that only extends up to 10 cm of path delay. For path delays of greater than 10 cm, this relationship should not be considered as accurate. In a similar fashion, neutral stability winds at 19.5 m above the ocean surface were retrieved from the altimeter radar cross section using a polynomial fit to the normalized radar cross section [7]

$$W = \sum_{i=0}^{4} a_i \sigma_0^i. \tag{10}$$

Applying all of these measurements and approximations to (6), the emissivity of the ocean surface can be estimated. An example of the results is shown in Fig. 1 at 18 GHz. In the figure, note for example the sharp increase in wind slope with the onset of foaming near 7 m/s.

Errors in each of the values used to derive the emissivity are summarized in Table II. The error in brightness temperature follows from [5]. A 1.1 K value for the error in T_u and T_d is conservatively chosen based upon [6]. Error in the opacity, derived from path delay, is taken as the root mean square error (RMSE) in the regression fit of the path delay versus opacity relationship. Ocean surface temperature was obtained from AVHRR measurements averaged over one month periods. The reported accuracy of individual temperatures [3] is such that the change of temperature from month to month is much greater than the error in any one month's average temperature. A variation in the surface temperature of 1.4 K was typical of the change in one month at the same location. The wind speed RMSE is a conservative value for wind speed retrieval based on satellite radar altimeter cross sections from TOPEX (Freilich and Challenor [9]). The error in path delay is the estimated error of the TOPEX path delay retrieval algorithm [5].

TABLE II
UNCERTAINTIES (1σ) IN THE DATA USED TO GENERATE THE OCEAN SURFACE EMISSIVITY

	18 GHz	21 GHz	37 GHz
T_B	1.7 K	2.1 K	1.9 K
T_u	1.1 K	1.1 K	1.1 K
T_d	1.1 K	1.1 K	1.1 K
τ	0.0014 Np	0.0012 Np	0.0051 Np
T_s	1.4 K	1.4 K	1.4
W	2.0 m/s	2.0 m/s	2.0 m/s
PD	1.5 cm	1.5 cm	1.5 cm

IV. ANALYSIS OF RESULTS AND DISCUSSION

The data sets (emissivity versus wind speed) are first placed into bins of 1 m/s. Next, a best-fit line is computed using the average values within each bin as the data points in the regression. The slope of the resulting best fit line is the wind slope. The region of low wind speed is considered first.

The wind slope predicted by [8] is 0.0005 s/m below 7 m/s, independent of frequency. Our results show wind slopes of 0.001 s/m for 18 and 21 GHz and 0.0015 s/m at 37 GHz when all data are included together.

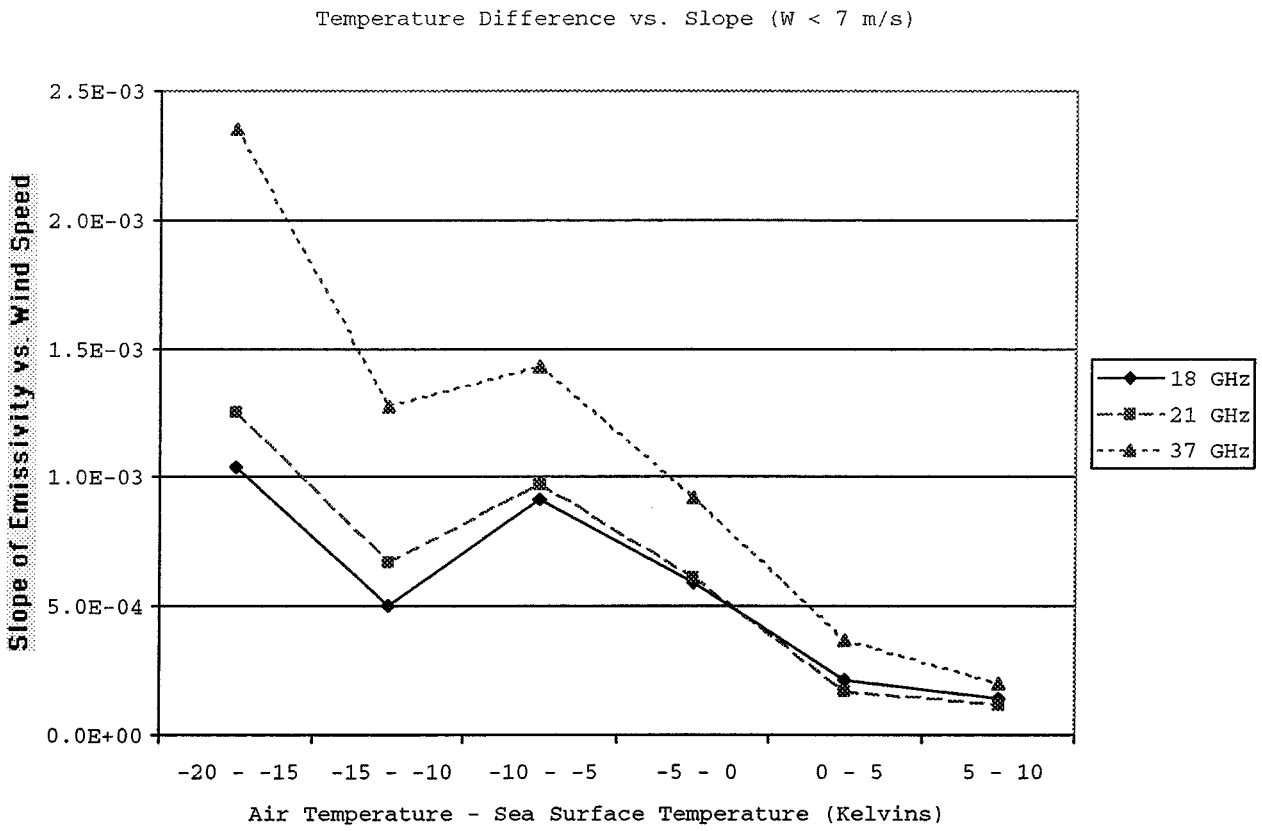

Fig. 2. Slope of emissivity versus wind speed as a function of the air-sea temperature difference for wind speeds less than 7 m/s.

In addition, a clear dependence of the wind slope on the sea surface temperature was noted. We conjecture that this behavior is likely the result of a dependence of sea state at a given wind speed on the atmospheric stability at the air–sea interface. No direct measurement was available of surface air temperature. To estimate the air temperature, path delay was used. In general, path delay is smaller at low temperatures because there is less moisture in the air. To model this behavior, a regression analysis was performed between path delay and surface air temperature, using a globally distributed set of 3000 island-based radiosonde profiles that were screened for clear sky and low path delay conditions. An exponential function was fit to this data yielding the model

$$T_{\text{surface\_air}} = 301 - 40.85e^{-0.1134(pd-0.5)} \tag{11}$$

where $T_{\text{surface\_air}}$ is in units of K, and pd is in units of cm. The residual RMSE in this regression fit is ~ 2 K.

To examine the dependence of wind slope on atmospheric stability, the data were sorted into 1 K bins by $\delta T = T_{\text{surface\_air}} - T_s$ before evaluating the wind slope. The results are shown in Fig. 2. Large negative values for δT, indicating significant instability, correspond with the largest values of wind slope. The wind slope decreases with increasing δT, dropping by $\sim 50\%$ under neutral stability conditions $(\delta T = 0)$ at 18 and 21 GHz and by $\sim 75\%$ at 37 GHz. Wind slope decreases even further, approaching zero under positive stability conditions $(\delta T > 0)$. These results can be interpreted as follows. The wind speed is estimated from the altimeter's radar cross section (RCS). The RCS at nadir incidence is most sensitive to long-wave perturbations from the specular condition (especially at the low wind speeds considered here). The emissivity, on the other hand, is most sensitive to short wave perturbations with scale size on the order of the electromagnetic wavelength. The dependence of the long wave magnitude and slope on wind speed will, in general, be much less affected by the atmospheric stability condition than will that of the short waves. This accounts for the general behavior seen here at all TMR frequencies. The fact that the emissivity at 37 GHz is much more sensitive to the stability condition is consistent with its smaller resonant wavelength being most effected by the stability condition (the authors would like to acknowledge the contribution by one anonymous reviewer to this interpretation of our results).

Above 7 m/s, with the onset of foaming, the dependence of wind slope on δT is found to diminish rapidly. The fractional foam model described by (1) and (2) satisfactorily describes the behavior of the data, provided an adjustment is made for the dependence of the underlying small wave variations on atmospheric stability. Since the contribution to excess emissivity by the foam tends to dominate that by the underlying small wave variations, the dependence on atmospheric stability becomes progressively smaller as wind speed increases. We also note here that an examination is currently underway of the dependence of wind slope on the relative angle between the wind direction and the polarization plane of the TMR observations, using other sources of wind vector data. There is a small but clear dependence. Therefore, the results presented here represent an average over all relative wind directions.

In addition to their contribution to understanding the behavior of the air–sea interface, these results should be useful for the development of water vapor retrieval algorithms used by nadir viewing radiometers on altimeter missions. This is especially the case for two-frequency radiometers, such as are flown on the ERS 1, 2, and GFO missions because of their greater need for a windspeed correction. In fact, early on-orbit validation work for the GFO Water Vapor Radiometer detected a windspeed dependent error in its water vapor estimates which was eliminated by use of this refined windspeed model [1].

ACKNOWLEDGMENT

The authors would like to thank the TOPEX Project Office, NASA Jet Propulsion Laboratory, California Institute of Technology,

Pasadena, CA for the use of their data. They would also like to acknowledge the useful comments by one anonymous reviewer.

REFERENCES

[1] J. C. Giampaolo, "An improved ocean surface emissivity wind speed correction," M.S. thesis, Pennsylvania State Univ., University Park, 1999.
[2] S. J. Keihm, V. Zlotnicki, and C. S. Ruf, "Topex Microwave Radiometer Performance Evaluation, 1992-1998," *IEEE Trans. Geosci. Remote Sensing*, no. 38, pp. 1379–1386, May 2000.
[3] E. P. McClain, W. G. Pichel, and C. C. Walton, "Comparative performance of AVHRR-based multichannel sea surface temperatures," *J. Geophys. Res.*, no. 90(C6), pp. 11 587–11 601, 1985.
[4] C. S. Ruf, S. J. Keihm, B. Subramanya, and M. A. Janssen, "TOPEX/Poseidon microwave radiometer performance and in-flight calibration," *J. Geophys. Res.*, no. 99, pp. 24 915–24 926, 1994.
[5] C. S. Ruf, "Detection of calibration drifts in spaceborne microwave radiometers using a vicarious cold reference," *IEEE Trans. Geosci. Remote Sensing*, no. 38, pp. 44–52, Jan. 2000.
[6] F. J. Wentz, "A model function for ocean microwave brightness temperatures," *J. Geophys. Res.*, no. 88, pp. 1892–1908, 1983.
[7] D. L. Witter and D. B. Chelton, "A GEOSAT altimeter wind speed algorithm and a model for altimeter wind speed algorithm development," *J. Geophys. Res.*, no. 96, pp. 8853–8860, 1991.
[8] T.T. Wilheit, "A model for the microwave emissivity of the ocean's surface as a function of wind speed," *IEEE Trans. Geosci. Remote Sensing*, vol. GE-17, pp. 244–249, 1979.
[9] M. H. Freilich and P. G. Challenor, "A model for the microwave emissivity of the ocean's surface as a function of wind speed," *J. Geophys. Res.*, vol. 99, pp. 25 501–25 062, 1994.

A Quantitative and Comparative Analysis of Linear and Nonlinear Spectral Mixture Models Using Radial Basis Function Neural Networks

Kerri J. Guilfoyle, Mark L. Althouse, *Member, IEEE*, and Chein-I Chang, *Senior Member, IEEE*

***Abstract*—A radial basis function neural network (RBFNN) is developed to examine two mixing models, linear and nonlinear spectral mixtures, which describe the spectra collected by both airborne and laboratory-based spectrometers. We examine the possibility that there may be naturally occurring situations where the typically used linear model may not provide the most accurate resultant spectral description. Under such a circumstance, a nonlinear model may better describe the mixing mechanism.**

***Index Terms*—Linear mixture, nonlinear mixture, radial basis function neural network (RBFNN).**

I. INTRODUCTION

Hyperspectral imaging spectrometers collect image cubes containing spectral data reflected from surface materials. Each pixel in an image cube contains the resultant mixed spectrum from reflected source radiation. This spectral data contain information about the component materials (endmembers) in the target region at the subpixel level. These imagers can be flown in either aircraft or on satellites and are used to study the endmember component structures of both terrestrial and planetary surfaces. The sensitivity ranges of these instruments typically lie between the visible and near-infrared ranges, for example, from 0.4 μm to 2.5 μm. The data collected by these spectrometers form an image cube that is typically on the order of 200 bands deep with complete images at each band. This paper investigates methods of interpreting such data cubes.

Historically, linear mixture models have been used to describe the resultant mixed spectra collected by hyperspectral imagers or laboratory-based spectrometers. However, it is also possible that a nonlinear mixture model may better describe the resultant mixture spectra for certain endmember distributions. It has been shown by Mustard and Pieters [1] that the use of a nonlinear mixture model that is based on Hapke's bidirectional spectroscopy theory [2], referred to as the intimate mixture model, improves abundance estimates in intimate mixtures of soils. In order to evaluate both of these mixing models, a tested set is developed in which both models can be easily applied and verified.

Linear mixture modeling is used to describe those situations in which the endmember components are distributed in block-like areas within the field-of-view (FOV) of the instrument. These situations may occur when the spectrometer FOV passes over discrete regions such as fields, lakes, rivers, and forests. In these cases, one would expect the resultant reflectance spectrum to be a linear combination of endmembers present in the region, for example, a river water component and perhaps a soil component (for the river bank). The linear model assumes that source radiation is singly reflected from the endmember substances and then collected by the imaging spectrometer.

Nonlinear mixtures occur in situations where endmember components are randomly distributed throughout the FOV of the instrument. Such situations may occur, for example, when viewing striated soils, in areas where multiple rock types are all visible on the region's surface, or in identifying trees in a forest (assuming reflectance spectra differences exist). In these cases, the resultant mixture reflectance spectrum may best be described by assuming that source radiation is multiply scattered by the randomly distributed endmembers before being collected by the imaging spectrometer. Experiments are conducted in such a manner that linear and nonlinear mixtures have been created with colored sand according to the above descriptions, and the resultant mixed spectra are analyzed. The results show that the nonlinear model does match the randomly distributed mixture spectra, while the linear model better matches the discrete region mixture [3].

In order to estimate the abundance of given endmember components using both models, a radial basis function neural network (RBFNN) is developed. It is based on a similar network designed by Leung and Lo [4] for the estimation of the angles of arrival of signals at an antenna. The Leung and Lo network was modified for abundance estimation by creating a test set using the known endmember data and comparing true mixture data with the test data.

II. SPECTRAL MIXTURE MODELS

In many current hyperspectral imagery applications, the spectrum of an image pixel is typically described by a linear mixture which can be modeled as a linear combination of image endmember components weighted by their abundance values as follows:

$$\mathbf{r} = \mathbf{M}\boldsymbol{\alpha} + \mathbf{n} \tag{1}$$

where

- $\mathbf{r}$ resultant spectrum of an image pixel vector with $\boldsymbol{\alpha}$ corresponding to the abundance column vector;
- $\mathbf{M}$ endmember spectra matrix;
- $\mathbf{n}$ noise vector.

Manuscript received April 11, 2000; revised September 7, 2000.

The authors are with the Remote Sensing and Image Processing Laboratory, Department of Computer Science and Electrical Engineering, University of Maryland, Baltimore County, Baltimore, MD 21250 USA (e-mail: cchang@umbc.edu).

Publisher Item Identifier S 0196-2892(01)05483-3.